



REU PROGRAM IN INTERDISCIPLINARY MATERIALS RESEARCH

Research Reports by Students Supported by
Cornell Center for Materials Research
(NSF MRSEC Program, DMR-1719875)

This REU Program for Interdisciplinary Materials Research is co-organized and co-supported by the REU Site for Interdisciplinary Materials Science (NSF REU Site Program, DMR-1757420) and the Cornell Center for Materials Research (NSF MRSEC program, DMR-1719875). This document contains the reports by all students that were funded by CCMR. The photo shows the cohort of the whole REU program. Students featured in this document are highlighted.



TABLE OF CONTENTS

Student

- 02 Cordelia Beck-Horton
- 06 Rebecca Meacham
- 10 Jamie North
- 16 Julio Rivera de Jesus
- 22 Collin Sanborn
- 27 Colleen Trainor
- 31 Dzmitry Vaido

Faculty Advisor

- Prof. Song Lin
- Prof. Alan Zehnder
- Prof. Chris Ober
- Prof. Chris Hernandez
- Prof. Brad Ramshaw
- Prof. Brett Fors
- Prof. Robert DiStasio Jr.

Electrochemical Dearomatization of Nitrogen Containing Heterocycles

Cordelia Beck-Horton and Song Lin

Being able to reduce heterocycles while tolerating other functional groups that can also be reduced is a sought after synthetic path. Rather than using dissolved metal catalysts, which are generally intolerant to functional groups, or relying on complex ring closing mechanisms, being able to directly functionalize and reduce a heterocycle would be a helpful development for organic synthesis. A method to make the reduction potential of a heterocycle less negative has been developed, as well as one to potentially dearomatize it.

Introduction

Dearomatization is a still growing field of organic synthetic chemistry. Dearomatization of heterocycles is of interest to develop because of the prevalence of dearomatized and/or functionalized nitrogen containing heterocycles in pharmaceutical molecules and other biologically active compounds. Improvement on the current standings on combining dearomatization with functionalization is being investigated by testing the possibility to electrochemically dearomatize a heterocycle at potentials tolerant of functional groups that are more susceptible to reduction than the aromatic system itself. By introducing an electron withdrawing group to the nitrogen of a heterocycle to decrease the electron density of the aromatic system, thus shifting its redox potential towards one more positive and making it easier to reduce, the possibility of a

higher functional group tolerance for those that are readily reduced in comparison with the unactivated heterocycle to survive through the reduction process when the heterocycle is activated becomes apparent. This has the potential to change how pharmaceutical and biological molecules are synthesized by allowing for functionalization of the heterocycle prior to reduction, followed by dearomatization. With development in tunability of the activating EWG, it is possible for selectivity in what functional groups are protected from reduction during dearomatization. But it all starts with electrochemically dearomatizing activated heterocycles.

Procedure

Activating Heterocycles

Each activation was done in a dry Schlenk flask under positive N₂(g) pressure. Stir bars were

added open to air and put under high vacuum and back filled with $\text{N}_2(\text{g})$ three times. All liquids were added with a needle and syringe through a rubber septum. Into the Schlenk flask, 15 mL of diethyl ether taken from an activated alumina column/argon atmosphere solvent system was added, followed by 5 mmol of quinoline. To -78°C , the flask was chilled before dropwise adding 1.1 equivalents of triflic anhydride. After allowing the flask to come back to room temperature, the precipitate was vacuum filtered in a $\text{N}_2(\text{g})$ glove box with diethyl ether dried over 3Å molecular sieves.

Electrolysis

All electrolyses were run in an oven dried glass cell with flame dried 3Å sieves, a scratched aluminum rod as the anode, and a stainless steel rod with a carbon felt tip as the cathode, under positive $\text{N}_2(\text{g})$ pressure. Any solids and stir bar were added open to air and put under high vacuum and back filled with $\text{N}_2(\text{g})$ three times. All liquids were added with a needle and syringe through a rubber septum. Into the cell, 5 mL of 0.5 M LiPF_6 in tetrahydrofuran was added, followed by 0.5 mmol of quinoline. The cell was chilled before adding 1.1 equivalents of triflic anhydride. After allowing the cell to come back to room temperature, 3

equivalents of 1,4-cyclohexadiene were added. Using a DC power supply, the cell had a potential of 31 V applied to it overnight.

Workup and Purification

The solvent of the reaction mixture of the electrolysis was removed under reduced pressure. The remaining solid was dissolved in ethyl acetate and washed with deionized water. The ethyl acetate layer was separated and evaporated. The remaining oil was dissolved in dichloromethane and run through an automatic gradient column from 88% hexanes and 12% ethyl acetate for 1 minute, with a ramp to 100% ethyl acetate over 10 minutes, and held at 100% ethyl acetate for 2 minutes. The fractions containing product were evaporated.

Characterization

Samples from activation were submitted for ^{19}F NMR in acetonitrile. Cyclic voltammograms were obtained in 0.1 M LiPF_6 in acetonitrile or 0.5 M LiPF_6 in tetrahydrofuran with a glassy carbon working electrode, a platinum wire counter electrode, and a 10 mM $\text{Ag}^+/\text{AgClO}_4$ reference electrode. Samples of the crude electrolysis mixture, the washed electrolysis mixture, and the purified electrolysis product were submitted for ^1H and ^{19}F NMR in deuterated dimethylsulfoxide.

Results and Discussion

The activated heterocycle's salt showed a new reductive event at approximately -1.2V vs 10 mM $\text{Ag}^+/\text{AgClO}_4$, while pure quinoline showed a peak only at -2.5V, showing that activation does in fact make the heterocycle easier to reduce.

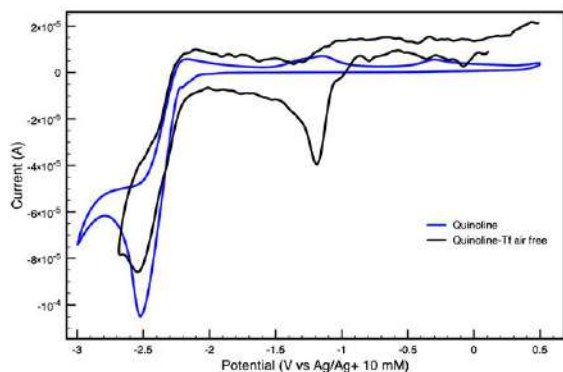


Figure 1. Cyclic voltammogram of quinoline in 0.1 M LiPF_6 in acetonitrile (blue trace), and of product of activated quinoline in 0.5M LiPF_6 in tetrahydrofuran.

The first attempts to activate the salt were done with triflic anhydride that had decomposed into triflic acid, protonating the heterocycle instead of adding an electron withdrawing group. After drying and distilling the triflic anhydride and redoing the synthesis, the activated salt was found to be very water and air sensitive, decomposing readily to a green paste, requiring a more rigorously air free procedure. Acetonitrile was observed turning the activated salt green when coming into

contact with it, so CV's were switched to be run in tetrahydrofuran rather than acetonitrile, as tetrahydrofuran was not observed decomposing the activated salt.

The NMR samples of the electrolysis crude and washed mixtures suggest the formation of a product, with the two ^{19}F peaks, suggesting a still substituted nitrogen, and the new aromatic ^1H peaks. The theoretical product, 1,4-dihydroquinoline, may be part of this mixture, which is also suggested since the oil obtained from the electrolysis was orange and when the compound was isolated in Synthesis of Heterocyclic Compounds by Ring-Closing Metathesis (RCM): Preparation of Oxygenated or Nitrogenated Compounds², it was reported as a yellow oil. The compound producing these signals hasn't yet been isolated, so an alternative method of isolation may be sought in the future.

Conclusion

Adding an electron withdrawing group to the nitrogen of a nitrogen containing heterocycle does change its redox behavior, and the activated compound reduces at approximately -1.2 V, about 1.3 V more positive than the non-activated heterocycle. The activated salt is very air and water sensitive, decomposing

readily. Forming this activated salt in situ for an electrolysis with 1,4-cyclohexadiene as a hydrogen atom donor appears to create a new compound which is possible to be 1,4-dihydroquinoline, but has yet to be isolated.

Acknowledgements

I would like to thank Dr. Song Lin for giving me the opportunity to do research with him for the summer, and Dr. Phillip Milner for providing his lab space and guidance in our labs collaborations. I would also like to thank José J. Fuentes-Rivera for mentoring me, the CCMR REU program for funding me for this summer's project, and the Cornell University NMR Facility (supported in part by the NSF through MRI award CHE-1531632).

References

1. Chénard, E., Sutrisno, A., Zhu, L., Assary, R. S., Kowalski, J. A., Barton, J. L., Bertke, J. A., Gray, D. L., Brushett, F. R., Curtiss, L. A., and Moore, J. S. (2016) Synthesis of Pyridine- and Pyrazine-BF₃ Complexes and Their Characterization in Solution and Solid State. *The Journal of Physical Chemistry C* 120, 8461–8471.
2. Pujol, M., and Sánchez, I. (2006) Synthesis of Heterocyclic Compounds by Ring-Closing Metathesis (RCM): Preparation of Oxygenated or Nitrogenated Compounds. *Synthesis* 2006, 1823–1828.
3. Wertjes, W. C., Southgate, E. H., and Sarlah, D. (2018) Recent advances in chemical dearomatization of nonactivated arenes. *Chemical Society Reviews* 47, 7996–8017.
4. Bull, J. A., Mousseau, J. J., Pelletier, G., and Charette, A. B. (2012) ChemInform Abstract: Synthesis of Pyridine and Dihydropyridine Derivatives by Regio- and Stereoselective Addition to N-Activated Pyridines. *ChemInform* 43.

Impact of water content in poly(vinyl alcohol) dual crosslinked hydrogel

Rebecca Meacham, Mincong Liu, Alan Zehnder

CCMR REU 2019

Abstract: Hydrogels are hydrophilic polymer networks that can be swollen with water when placed in solution. Traditional single-network hydrogels typically have poor mechanical strength leading to limited uses. Dual crosslinked hydrogels have both chemical and physical crosslinks. This improves the mechanical properties of the gel and can mimic those of cartilage, so they have potential biomedical applications. Poly(vinyl alcohol) dual crosslinked hydrogels have been studied previously. The PVA gel contains about 90% water when fully saturated. The effect of the water content in the PVA gel has not yet been investigated. By altering the relative humidity, the drying rate of the gel can be observed. The impact of the water content can be measured by standard mechanical tests at different saturations. Additionally, the diffusivity of water in the gel can be calculated by constricted swelling tests.

Introduction

Hydrogels are polymer networks that are able to absorb water. Typically, synthetic hydrogels are brittle and have low mechanical strength when swollen. To overcome this, more complex polymer networks have been introduced to create hydrogels with better mechanical properties. Double network gels are an example. Double network gels contain two polymer networks that are intertwined to form one hydrogel network¹. This type of gel was made to improve the mechanical strength of hydrogels which allows for use in biomedical applications such as artificial cartilage or other tissues.

The high mechanical strength of double network gels comes from selecting the two polymer networks such that one network will break when a load is applied. This dissipates energy in the gel and allows the second network to continue to be loaded. The limitations to these gels include the irreversible damage caused by the failure of the first network. To overcome this, a dual crosslinked gel was created². Instead of having two polymer networks as in a double network gel, dual crosslinked gels have one polymer network that is crosslinked both chemically and physically. The physical crosslinks act as the breakable network to dissipate energy. Unlike the double network gels, once the physical bonds are broken and the energy is dissipated, new physical bonds can be formed to heal the material.

Previously, dual crosslinked poly(vinyl alcohol) (PVA) hydrogels have been studied³. The mechanical properties of this gel have been studied

at varying temperatures and loading rates, but always when the gel was nearly saturated. By studying the effect of water content on the gel, the behavior of the gel under different conditions can be further understood.

The diffusivity of a material is often used to determine the effect of the poroelasticity of hydrogels. This describes how fast water or solvent moves through the material. One way to determine the diffusivity of a gel is by swelling the material and measuring the change in volume⁴. To simplify the calculations, swelling can be constricted to one dimension. This also simplifies the measurement of the change in the volume of the gel to only the change in the thickness of the gel. Swelling of the gel can then be modeled by the equation

$$\frac{\Delta(t)}{H} = \frac{2\Delta(\infty)}{H^2} * \sqrt{\frac{D*t}{\pi}} \quad (1)$$

where $\Delta(t)$ is the change in thickness, H is the initial thickness, $\Delta(\infty)$ is the equilibrium change in thickness, D is the diffusivity, and t is time.

By plotting the normalized change in thickness and square root of time divided by the initial thickness, a linear relationship can be achieved. The slope of the linear portion, k , can be used to calculate the diffusivity:

$$D = \pi * \left(\frac{k*H}{2\Delta(\infty)}\right)^2 \quad (2)$$

Methods

PVA hydrogel was made in three steps. First a 16% PVA solution was made by combining PVA and distilled water. Then the PVA solution was chemically crosslinked with glutaraldehyde under acidic conditions with hydrochloric acid for 24 hours. The gel was washed to neutralize the pH. Finally, the physical crosslinks were introduced by soaking the gel in an ionic solution for three days. The ionic solution contained water, sodium chloride, and borax. The gel remained in the solution for up to 2-3 weeks while being used. The final gel contained approximately 12% PVA and the balance ionic solution. Samples of the gel were cut from a sheet to be tested.

Drying experiments were done in a chamber to control the temperature and relative humidity. The gel was placed on a screen in the chamber to allow air flow above and below the sample. The temperature was held at 24°C for all drying experiments. The relative humidity was held at 20%, 40%, 60%, and 80%. The actual humidity varied from 20%-30% during testing at the 20% setpoint due to the limits of the chamber. At higher humidity levels the setpoint values were accurately attained.

Mechanical testing was done using a tensile instrument. Three standard tests were done to determine the properties of the gel. The first two tests were load/unload cycles at constant stretch rates of 0.01/s and 0.005/s. The gel was pulled to a stretch of 1.3, or to 130% of the original length, at both rates and then unloaded at the same rate. The third test was a stress relaxation test. The gel was pulled to a stretch of 1.3 at a fast rate and held in the stretched state for 20 minutes. From these tests, the effect of water content in the gel on the mechanical properties was determined.

All mechanical tests were done with one sample. The sample remained in the test set up for the duration of the tests. One hour passed between each set of tests to allow drying to occur. A reference sample was kept and weighed to determine the remaining mass of the gel being tested. After the duration of the tests, the tested sample was weighed. The total weight loss of the

tested and reference samples varied by an insignificant amount.

Constricted swelling experiments were done with partially dried gel. The gel was dried in the chamber at 60% relative humidity and 24°C for approximately 45 minutes, until the weight of the gel was around 80% of the original weight. The gel was then cut into a disc and placed in a tube in the ionic solution to swell. The experimental set up is pictured in figure 1. From the change in thickness while swelling, the diffusivity was calculated using equation 2.

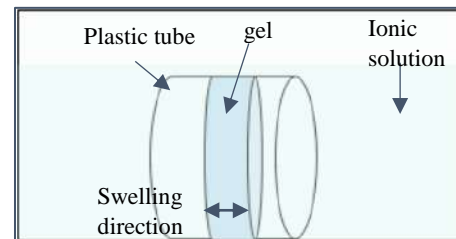


Figure 1: Experimental setup for constricted swelling test

Because of the soft nature of the gel, the thickness of the gel cannot be easily measured using calipers. Instead, an optical lens and translational stages were used to measure the thickness of the gel. The gel was mounted vertically on a glass slide and viewed through the lens as the thickness was measured by the movement of the stage.

Discussion

Before mechanical testing was done, the effect of relative humidity and the drying rate of the gel needed to be determined. Gel samples were dried in a chamber at different values of relative humidity. The results show that the gel dried linearly with time initially. The drying rate decreased exponentially until the dry weight was reached and there was little to no solution remaining. The drying rate decreased as the relative humidity increased, as expected (Figure 2). In more saturated air conditions, there is less of a gradient of moisture concentration between the gel and the air, so diffusion of the ionic solution out of the gel was slowed.

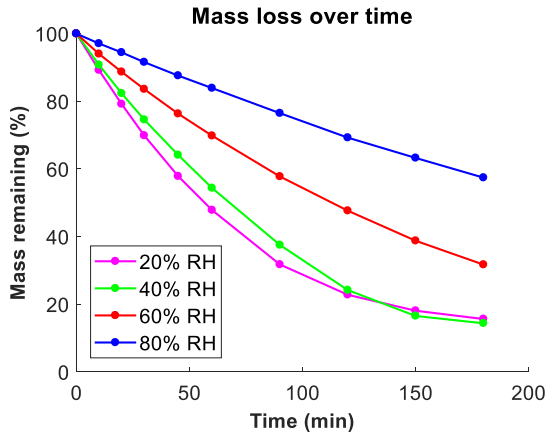


Figure 2: Mass loss over time at 20%, 40%, 60% and 80% relative humidity

Mechanical testing was done to determine the effect of water content on the mechanical properties of the gel. Figures 3A and B plot the nominal stress (force/initial cross sectional area) vs the stretch. Figure 3C plots the nominal stress vs time. The data all show an increase in stiffness of the gel as it dries. The first and second tests showed an increase of peak stress as the gel dried (Figure 3A, 3B). At a loading rate of 0.01/s the peak stress increased from 6000 N/m² when fully saturated to 10000 N/m² after 3 hours of drying. Similarly, at a loading rate of 0.005/s, the peak stress increased from 5000 N/m² to 9000 N/m² after being dried. From the stress relaxation tests, an increase in stiffness can be seen by an increase in peak stress (Figure 3C). The plateau stress also increased as the gel dried.

The mass of the gel decreased by about 25% during the tests. The mass loss is assumed to be completely due to the loss of the ionic solution, meaning that the water content in the gel also decreased by 25%.

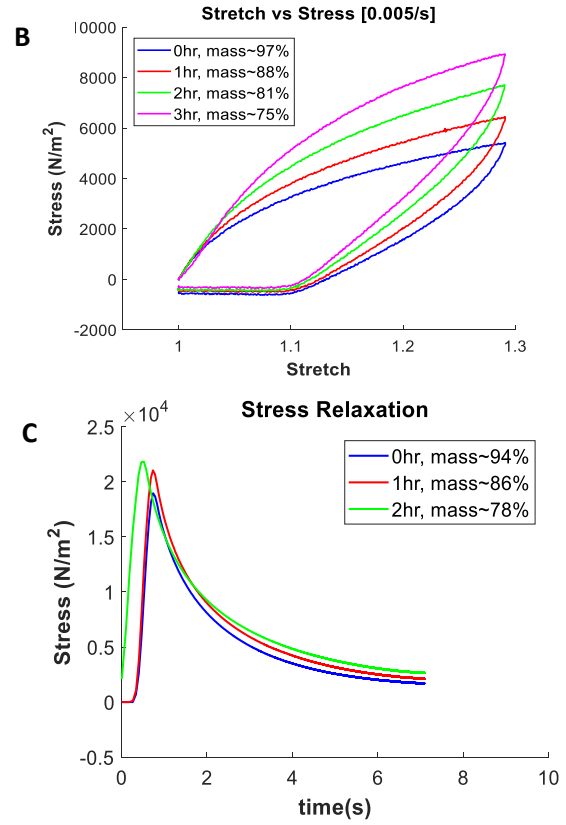
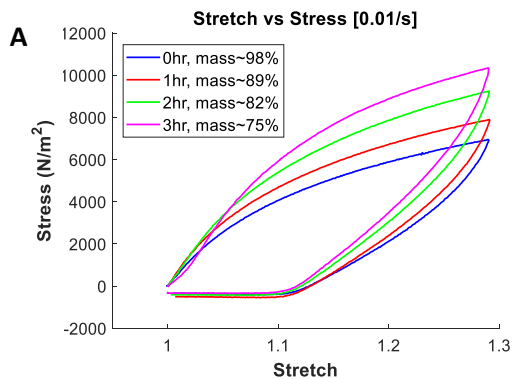


Figure 3: Mechanical test results from load/unload at 0.01/s (A), load/unload at 0.005/s (B), and stress relaxation (C).

The constricted swelling tests were done to determine the diffusivity of the ionic solution in the gel. The normalized thickness was plotted with the square root of time (in seconds) divided by the original thickness, H . The relationship was initially linear, but then reached a plateau as the original, swollen thickness was reached. Figure 4 shows the average of five thickness measurements for each time. There was a large scatter between the measurements possibly due to the lack of precision of the thickness measurements and the small changes. A line was fit to the first 30 minutes of swelling data to calculate the diffusivity using equation (2) with $\Delta(\infty) = 0.2$ mm. This value was chosen because the gel was dried to 80% of the original weight, so it was assumed that the gel thickness also decreased by 20% of the original thickness. The diffusivity of the ionic solution in the gel was calculated to be $4 \times 10^{-9} \text{ m}^2/\text{s}$.

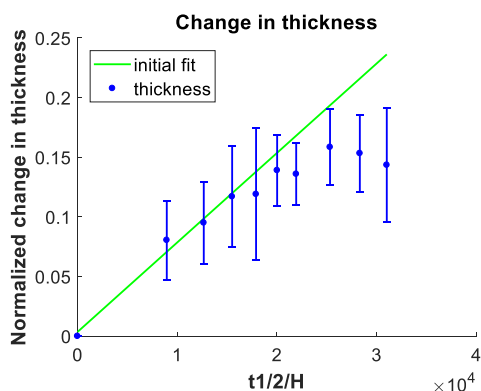


Figure 4: The normalized change in thickness from the constricted swelling test plotted against the square root of time (in seconds) divided by the initial thickness. The line represents a linear fit for the first 4 data points.

Conclusions

The impact of water content on a PVA dual crosslinked gel was investigated. The PVA gel dried exponentially with different rates at different values of relative humidity. As the gel dried, it became stiffer. The diffusivity of the gel was calculated and was similar to values for other hydrogels. From this data, the behavior of the gel under different conditions can be further understood.

Acknowledgements

Thank you to Professor Zehnder and Mincong for their guidance and mentorship as well as the CCMR and NSF for supporting this work.

References

1. J.P. Gong, Y. Katsuyama, T. Kurokawa, Y. Osada, Double-Network Hydrogels with Extremely High Mechanical Strength, *Adv. Mater.* 15 (14) (2003) 1155-1158
2. K. J. Henderson, T. C. Zhou, K. J. Otim, K. R. Shull, Ionically Crosslinked Triblock Copolymer Hydrogels with High Strength
3. M. Liu, J. Guo, C-Y. Hui, C. Creton, T. Narita, A. Zehnder, Time-temperature equivalence in a PVA dual cross-link self-healing hydrogel, *Journal of Rheology*, 62 (991) (2018) 991-1000
4. J. Yoon, S. Cai, Z. Suo, R. Hayward, Poroelastic swelling kinetics of thin hydrogel layers: comparison of theory and experiment, *Soft Matter*, 6 (2010) 6004-6012

Synthesis of Magnetic Nanoparticles for Creation of Polymer-Grafted Nanoparticle Arrays

Jamie North, Nick Diaco, Florian Käfer, Christopher K. Ober

Abstract

Magnetic nanoparticles such as iron ferrite (Fe_3O_4) and cobalt ferrite (CoFe_2O_4) have unique magnetic properties that make them desirable as cores for the synthesis of polymer-grafted nanoparticles (PGNs) and the preparation of monolayers and 2D arrays. In this respect, the dispersibility of the nanoparticles (NPs) in aqueous solutions and their particle size distribution plays an important role. The synthesis of these NPs through formation of an oleate complex and subsequently stabilization with oleic acid as ligand enables the leads to the formation of monodisperse NPs with a diameter of 14 nm. In contrast, the synthesis of CoFe_2O_4 using a coprecipitation method from metal chlorides produces aggregated clusters of nanoparticles, which are eventually not appropriate for the production of PGNs and 2D arrays with a long-range order.

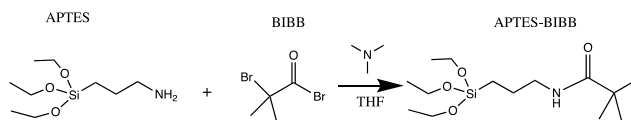
Introduction

In recent years, Organic-Inorganic Hybrid Nanoparticles (OIHNs) have caught the attention of both academia and industry since well-established classes of materials, such as metals, polymers, and ceramics, are limited in their properties. PGNs, in particular, are unique in their capacity to interact with neighboring PGNs via brush entanglement and interactions, enhancing their thermal, mechanical and electrical properties compared to their single-component counterparts.^{1, 2} PGNs can be used for the preparation of desired architectures in applications such as sensors, biohybrid materials, and photonic devices. For the creation of polymer canopies, proton donor polymers, such as poly(methacrylic acid) (PMAA) and poly(acrylic acid) (PAA), will have unique interparticle interactions with proton acceptor polymers, such as poly(*n*-vinyl pyrrolidone) (PNVP). Use of magnetic cores in creating these PGNs can create materials with unique magneto-optic properties, which are of particular use in creating faraday rotators. Unlike in other polarization devices, faraday rotators do not produce back reflected polarized light,

making them ideal for creation of isolators of polarized light.

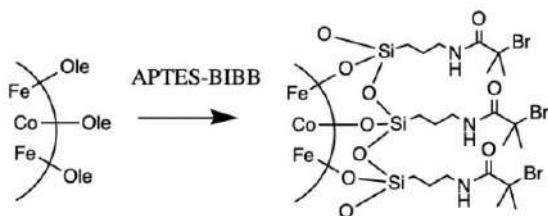
In this project, we aimed to create PGNs by attaching an Atom Transfer Radical Polymerization (ATRP) initiator to magnetic metal-oxide NPs and growing a homogeneous polymer corona.³ The types of nanoparticles we were investigating were silica (SiO_2), iron ferrite (Fe_3O_4), and cobalt ferrite (CoFe_2O_4), typically of a size between 10 and 40 nm. In the ferrites, the particles have a B(AB)O_4 structure, which is known as an inverse spinel structure and their unusual magnetic properties. A has a 2+ oxidation state and occupies the octahedral sites and half of the tetrahedral sites whereas B has 3+ oxidation state and occupies the other half of the tetrahedral sites. Cobalt is the A metal and iron is the B metal in cobalt ferrite, whereas in the iron ferrite the iron takes both oxidation states.¹ Within the NP the metals form complexes with the oxygens, while the surface the metals can coordinate to either hydroxide or water. Replacing these coordinating groups was how we aimed to functionalize these particles with an ATRP imitator.

The initiator connector we used was APTES-BIBB (3-aminopropyltriethoxysilane-2-bromoisobutryl bromide), which we synthesized using APTES and BIBB in THF, with triethylamine to neutralize the produced HBr [Scheme 1]. The initiator structure was confirmed by ¹H-NMR.

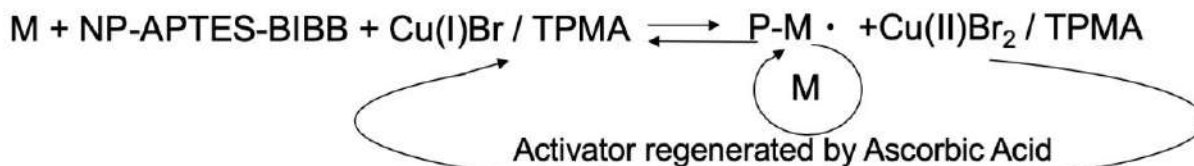


Scheme. 1 Synthesis of the ATRP initiator APTES-BIBB for the functionalization of the NPs.

The siloxane has been shown to coordinate to the surface of the nanoparticle by hydrolyzing the ethyl groups and then undergoing condensation reactions to form either uniform or multilayers. The three alkoxide groups enable it to act as a more effective chelating ligand, replacing the ligands already on the surface [Scheme 2].



Scheme. 2 Functionalization of the CoFe₂O₄ APTES-BIBB.



Scheme. 3 Mechanism of ARGET-ATRP using APTES-BIBB functionalized NPs.

When we were certain the particles were at least mostly dispersed, accurate sizes were obtained using transmission electron microscope (TEM). Thermogravimetric analysis (TGA) was used to determine the polymer weight percent (wt%) of the PGNs.

These NPs can be used for the polymerization of different monomers using ATRP as the synthesis technique. During the ATRP, Cu(I)Br will be oxidized to Cu(II)Br₂ and a radical on the tertiary carbon is formed. This radical is then available to react with the vinyl group of the monomer, but this reaction is driven to the Cu(I)Br, temporarily capping the radical with Br and slowing the polymerization. This polymerization is fairly stable for a radical polymerization; the ATRP method reduces the risk of chain transfer and premature termination. By adding a small amount of Cu(II)Br₂ to solution and then reducing it slowly with ascorbic acid, we are able to control the rate of polymerization, enabling the producing of regular chain lengths. This type of ATRP is called Activator regenerated electron transfer (ARGET) [Scheme 3].

To characterize these PGNs, dynamic light scattering (DLS) was used to determine the hydrodynamic radius. As DLS gives sizes to order of magnitude accuracy, DLS was used to determine whether the particles were aggregating into large clusters.

Methods

Materials

The syntheses of NPs and initiator were carried out using commercially available reagents. CoFe₂O₄ nanoparticles, FeCl₃ (>99%), CoCl₂ (>99%), sodium hydroxide,

sodium oleate (>97%), oleic acid (>90%), CuBr₂ (99.999%), ascorbic acid, TPMA (98%), ethanol, hexane, 1-octadecene (>90%), APTES (99%), BIBB (98%), THF, dichloromethane, NVP, Acrylic acid, MAA, triethylamine (>99%), sodium bicarbonate, and magnesium sulfate were all purchased from Sigma Aldrich. NVP, acrylic acid, and MAA were all distilled before use. All other reagents were used as arrived.

Synthesis of Cobalt Ferrite Nanoparticles through Coprecipitation

The coprecipitation technique was adapted from Chinnasamy⁵, Liu⁶ and Khan⁷. The metal nanoparticles were prepared through a reaction of metal salts in basic solution. A 15 mL solution of 0.1 M cobalt (II) chloride, 0.2 M iron (III) chloride, and 0.4 M hydrochloric acid was added to 1.5 L of deionized water and stirred. The solution was heated to 80°C. 76 mL of 20 M sodium hydroxide was added dropwise to the reaction vessel over 5 minutes. The solution was then stirred for 2 hours at temperature, and the product was purified through washing with water and centrifuging 3 times. Yield after freeze drying was 2.6 g.

Synthesis of the Metal Oleate Complex

This technique of oleate synthesis of the nanoparticles was modified from Baos and Park.⁹ The alternative method of preparing nanoparticles involved creating a metal oleate complex, and then reacting it at 320°C with oleic acid. This method was used to produce both iron ferrite and cobalt ferrite nanoparticles. 1.08 g of iron (III) chloride hexahydrate (0.72 g of iron (III) chloride hexahydrate and 0.36 g of cobalt (II) chloride hexahydrate was used in the preparation of cobalt ferrite) was added to 14 mL of hexane, 8 mL of ethanol, and 6 mL of water. 3.69 g of sodium oleate was added, the mixture was stirred under argon at 70°C for 4 hours. The produced organic layer was washed 3 times

with 30 mL of water in a separatory funnel and was freeze dried to produce an oily solid.

Synthesis of the Nanoparticles from the Metal Oleate Complex

Solid from oleate complex synthesis was dissolved in 20 g of 1-octadecene with 0.87 g of oleic acid. The solution was heated to 320°C in a salt bath (7% NaNO₃, 40% NaNO₂, 53% KNO₃) for 1 hour. The product was added to a large excess of ethanol, which precipitated the nanoparticles as an oily solid. The result was soaked in excess ethanol 3 times before being dried by freeze drier,

Synthesis of APTES-BIBB initiator

25.7 mL of APTES was stirred with 42.2 mL triethylamine in 550 mL tetrahydrofuran (THF). 18.7 mL of BIBB was added to the reaction solution in 100 mL THF. After stirring the solution over night, the precipitate was removed by filtration and THF was removed under reduced pressure. The crude product was dissolved in dichloromethane (DCM) and washed four times with a saturated sodium bicarbonate solution and with water subsequently. The organic layer was collected and dried using MgSO₄. DCM was removed under reduced pressure and the crude product was filtered before stored at -20°C.

Addition of APTES-BIBB initiator

The addition of initiator in hexane was adapted from De Palma¹⁰ and the addition in ethanol was adapted from Kang.¹¹ Particles were dispersed at a concentration of between 1-10 mg/mL in two different solvents depending on the synthesis technique. Particles generated from coprecipitation were dispersed in ethanol at 10 mg/mL, and particles generated from oleate synthesis were dispersed in hexane at 1.4 mg/mL. 16 g of APTES-BIBB was added for every gram of NP. In ethanol, the reaction was heated to 50°C and stirred overnight. In hexane, the

reaction was stirred for 72 hours at room temperature. The particles were purified by dialysis in the same solvent and freeze drying.

ATRP Polymerization of NPs

271 mg of CoFe_2O_4 was dispersed in 10 mL of water through repeated vortexing and sonication. This solution was added to 43.2 mL of water containing 12.2 mg of tris(2-pyridylmethyl)amine (TPMA) and 1 mL of CuBr_2 solution (1 mg/mL). 3.6 mL of the chosen monomer, either methacrylic acid (MAA), acrylic acid (AA), or n-vinyl pyrrolidine (NVP), was added to the solution. This solution was bubbled with argon for 10 minutes and was heated to 80°C and stirred. 3.6 mL of ascorbic acid (2 mg/5 mL) was added over 6 hours using a syringe and a syringe pump. The product was purified by dialysis in water. Fe_3O_4 particles followed the same procedure, but at a ratio of 1.012 g Fe_3O_4 NPs per 1 g CoFe_2O_4 NPs to account for density.

Results and Discussion

Initial particles used were following the synthesis of the coprecipitated nanoparticles, both these and particles purchased from Sigma Aldrich were attempted to be dispersed in water before attempting to attach the ATRP initiator. The Sigma-Aldrich particles were unable to be dispersed in water. DLS was used to confirm that the particles were aggregating on the $1\ \mu\text{m}$ scale. The CP NPs appeared to be dispersed in solution, with a hydrodynamic radius of 27.6 nm (DLS). However, they were shown to be aggregated by TEM (Figure 4). Attempts to initialize and polymerize these particles were ineffective; they aggregated in the reaction solution before any polymerization could take place.

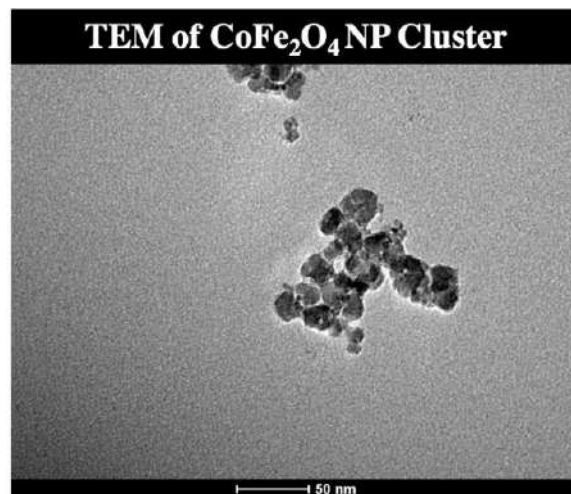


Fig. 4 Synthesized CoFe_2O_4 NPs using coprecipitation (CP).

The coprecipitate method was abandoned at this point, and batches of both Fe_3O_4 and CoFe_2O_4 were synthesized through the oleic acid method. These particles were found to be well dispersed as shown by DLS and TEM, see Figure 5. The Fe_3O_4 NPs had an average size of 14.3 nm with a standard deviation of 2.4 nm, and the CoFe_2O_4 NPs had an average size of 14.9 nm with a standard deviation of 2.5 nm (Figure 5). The NPs were also found to arrange in monolayers when deposited from evaporating hexane. These particles were successfully used for the polymerization of poly(N-isopropylacrylamide) (PNiPAAm).

Conclusion

The ATRP imitator APTES-BIBB was successfully synthesized and grafted to magnetic Fe_3O_4 and CoFe_2O_4 nanoparticles. The preparation of CoFe_2O_4 using coprecipitation was resulting in aggregation of the obtained NPs. In contrast, using a thermal decomposition synthesis route with oleic acid as the ligand, monodisperse and easy dispersible Fe_3O_4 and CoFe_2O_4 NPs with a diameter of 14 nm were obtained. In order to manufacture functional PGNs-monolayers and 2D arrays further experiments are required.

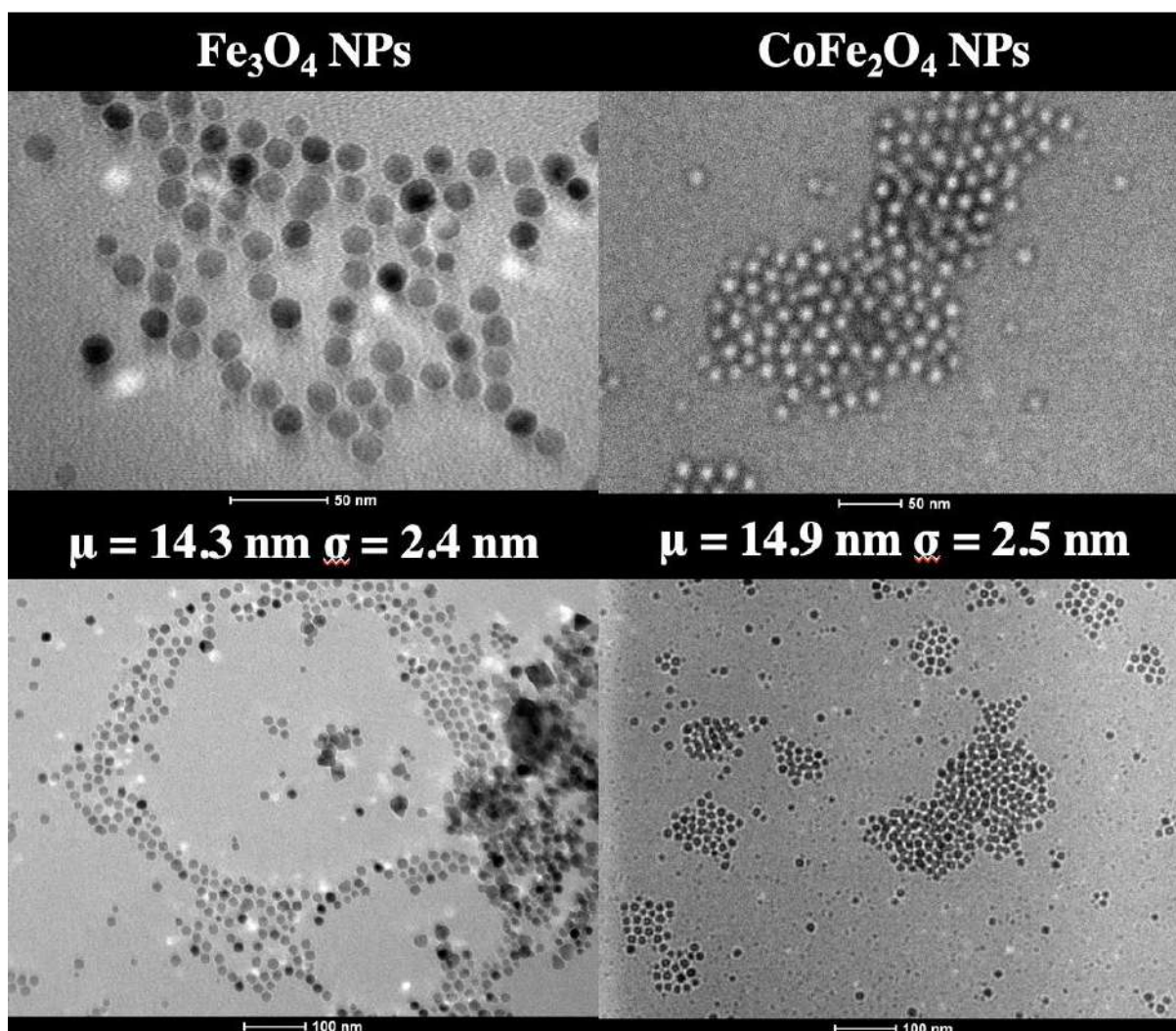


Fig. 5 TEM of Fe_3O_4 (left) and CoFe_2O_4 (right) nanoparticles at high magnification (top) and low magnification (bottom). The particles are dispersed and are seen forming monolayers, especially the CoFe_2O_4 . The average size (μ) and standard deviation (σ) are shown in the center.

Acknowledgements

I would like to thank Prof. Christopher Ober for offering me the opportunity to work in his lab for the summer, as well as Dr. Florian Käfer for his excellent mentorship throughout the CCMR REU. I would also like to thank Nick Diaco for being a great partner in this research. Additional thanks to the Ober Group members for all the help they provided learning the techniques of the lab. A special thanks to the CCMR REU program for making this experience possible.

Funding

This work was supported by the Cornell Center for Materials Research with funding from the Research Experience for Undergraduates program (DMR-1757420 and DMR-1719875). This work was performed in part at the Cornell Nanoscale Facility, a member of the National Nanotechnology Coordinated Infrastructure (NNCI), which is supported by the National Science Foundation (Grant NNCI-1542081).

References

- Francis, R.; Joy, N.; Aparna, E. P.; Vijayan, R. Polymer Grafted Inorganic Nanoparticles, Preparation, Properties, and Applications: A Review. *Polymer Reviews* **2014**, 54 (2), 268-347 DOI: 10.1080/15583724.2013.870573.
- Fernandes, N. J.; Koerner, H.; Giannelis, E. P.; Vaia, R. A. Hairynanoparticle assemblies as one-component functional polymer nanocomposites: opportunities and challenges. *MRS Communications* **2013**, 3 (1), 13-29 DOI: 10.1557/mrc.2013.9.
- Liu, Y.; Li, Y.; Li, X.-M.; He, T. Kinetics of (3-Aminopropyl)triethoxysilane (APTES) Silanization of Superparamagnetic Iron Oxide Nanoparticles. *Langmuir* **2013**, 29 (49), 15275-15282 DOI: 10.1021/la403269u.
- Houshiar, M.; Zebhi, F.; Razi, Z. J.; Alidoust, A.; Askari, Z. Synthesis of cobalt ferrite (CoFe₂O₄) nanoparticles using combustion, coprecipitation, and precipitation methods: A comparison study of size, structural, and magnetic properties. *Journal of Magnetism and Magnetic Materials* **2014**, 371, 43-48 DOI: <https://doi.org/10.1016/j.jmmm.2014.06.059>.
- Chinnasamy, C.; Jeyadevan, B.; Perales, O.; Shinoda, K.; Tohji, K.; Kasuya, A. Growth dominant co-precipitation process to achieve high coercivity at room temperature in CoFe₂O₄ nanoparticles. *Magnetics, IEEE Transactions on* **2002**, 38, 2640-2642 DOI: 10.1109/TMAG.2002.801972.
- Liu, F.; Laurent, S.; Roch, A.; Vander Elst, L.; Muller, R. Size-Controlled Synthesis of CoFe₂O₄ Nanoparticles Potential Contrast Agent for MRI and Investigation on Their Size-Dependent Magnetic Properties. *Journal of Nanomaterials* **2013**, 2013, 1-9 DOI: 10.1155/2013/462540.
- Khan, M.; Mumtaz, A.; Hasanain, K.; Ceylan, A. Synthesis and Magnetic Properties of Cobalt Ferrite (CoFe₂O₄) Nanoparticles Prepared by Wet Chemical Route. *Journal of Magnetism and Magnetic Materials* **2006**, 308, 289-295 DOI: 10.1016/j.jmmm.2006.06.003.
- Bao, N.; Shen, L.; An, W.; Padhan, P.; Heath Turner, C.; Gupta, A. Formation Mechanism and Shape Control of Monodisperse Magnetic CoFe₂O₄ Nanocrystals. *Chemistry of Materials* **2009**, 21 (14), 3458-3468 DOI: 10.1021/cm901033m.
- Park, J.; An, K.; Hwang, Y.; Park, J.-G.; Noh, H.-J.; Kim, J.-Y.; Park, J.-H.; Hwang, N.-M.; Hyeon, T. Ultra-large-scale syntheses of monodisperse nanocrystals. *Nature Materials* **2004**, 3 (12), 891-895 DOI: 10.1038/nmat1251.
- De Palma, R.; Peeters, S.; Van Bael, M. J.; Van den Rul, H.; Bonroy, K.; Laureyn, W.; Mullens, J.; Borghs, G.; Maes, G. Silane Ligand Exchange to Make Hydrophobic Superparamagnetic Nanoparticles Water-Dispersible. *Chemistry of Materials* **2007**, 19 (7), 1821-1831 DOI: 10.1021/cm0628000.
- Kang, M. K.; Mao, W.; Yoo, H. S. Surface-initiated atom transfer radical polymerization of cationic corona on iron oxide nanoparticles for magnetic sorting of macrophages. *Biomaterials Science* **2018**, 6 (8), 2248-2260 DOI: 10.1039/C8BM00418H.

The Effect on the Mechanical Properties of Bone Tissue in Type II Diabetes Mice when exposed to *Faecalibacterium Prausnitzii*.

Julio A. Rivera- de Jesus^{1,2}, Macy Castaneda², Christopher J. Hernandez^{2,3}

¹Department of Chemical Engineering, University of Puerto Rico Mayaguez; ²Sibley School of Mechanical and Aerospace Engineering, Cornell University; ³Meinig School of Biomedical Engineering, Cornell University

Abstract

The gut microbiome consists of more than thousands of microbial species acquired at the moment of birth and is unique to every person. Most of the human microbiome is located in the gastrointestinal system, called the gut flora. Recent studies have shown a correlation between the gut microbiome and whole bone mechanical properties. It is clear that altering the gut microbiome affects bone growth and bone quality, but the mechanistic pathways that determine changes in bone are not yet well understood. A previous study demonstrated that *Faecalibacterium prausnitzii* can alter the gut microbiome. Disease states also alter bone properties; specifically, type II diabetes (T2D) patients present higher fracture risk. Continuing this line of thought we proposed to alter the gut microbiome in type II diabetic mice and assess the changes in the mechanical properties of the bones. Moreover, *F. prausnitzii* is directly linked to T2D for its ability to maximize adiponectin expression and increase insulin sensitivity. Preliminary results show that mice orally exposed to *F. prausnitzii* presented an increase in cross sectional area and moment of inertia. Data suggests that *F. prausnitzii* could be inducing higher bone mineral density and stimulating bone formation.

Introduction

The human microbiome is a complex ecosystem of bacterial microorganisms. The composition of the microbiome varies across body sites[1]. The gut microbiome is the concentration of the human microbiome located at the gut[2]. The gut microbiome is initially obtained at birth and undergoes alterations throughout the life span of the host due to diet[3] and environment[4]. It is known that there are certain patterns in the microbiome composition that describe a diseased state. Thus, altering the gut microbiome can lead to inflammatory bowel disease, ulcerative colitis, and type II diabetes [5], [6]. In this study, we focus on how the microbiome could be affecting

cortical whole bone structure and density as well as the mechanical properties of cortical bone tissue.

Mice models have been proven to be greatly useful to study skeletal biology.

Biomechanical principles of long bones can accurately be determined by a single load mechanical test [7] called 3-point bending. The mechanical properties of the femur can be calculated using beam theory. Previous studies have also studied bone fracture by assuming the mid-diaphysis to be a uniform cylindrical pipe[8]. For this study, we focused on values for peak bending moment and tissue strength.

Faecalibacterium prausnitzii (FP) is the most abundant bacteria in the human gut

microbiome, accounting for more than %5 of the total bacteria population. Moreover, *F. prausnitzii* is known to be an indicator of intestinal health, primarily due to its ability to produce butyrate[9]. Low concentrations of *F. prausnitzii* commonly result in the alteration of the gut microbiome and has consequently influenced diseases like: inflammatory bowel disease, Crohn's disease, ulcerative colitis and type II diabetes[5].

From previous studies, we know that the gut microbiome composition in mice models will influence the accumulation of bone mass during their lifespan[10]. We also know that alterations in the gut microbiome contribute to a number of conditions that could negatively affect the bone by inducing bone mass loss or increase fracture risk[2]. Due to past studies, we propose to study the bone tissue mechanical properties in type II diabetes mice, who present higher fracture risk[11], and were also orally exposed to *F. prausnitzii*. With previous knowledge on *F. prausnitzii*, we hypothesize that this probiotic will decrease fracture risk and consequently stimulate healthier bone formation.

2.Methods

2.1 Animals

C57B/6J mice were purchased from Jackson Laboratories and were bred in Cornell University's Animal Facility. At the age of 4 weeks, mice were separated randomly into three groups with different dietary treatments for 12 weeks: group 1 (n=7) high fat diet (HFD) and exposed to *F. prausnitzii* every other week, group 2 (n=16) high fat diet, and group 3 (n=7) control chow. Animals were weighted every 2 weeks. Thereafter, animals were euthanized via

cardiac puncture and tissue samples were collected. Fat Pad Mass was weighed. Right and left femoral bones were extracted and stored at -20° Celsius for μ CT scan and mechanical testing.

2.2 Mechanical testing

Femoral bones were thawed at room temperature before analysis. Whole bone strength and tissue strength of the cortical bone tissue were measured using a 3-point bending test on an MTS 858 Mini Bionix. Bones were placed and centered on a fixture with a 5.33mm span length. A loading rate of 0.1mm/s was applied until samples reached mechanical failure.

2.3 Image processing

Cross sectional area (CSA) of dissected femoral bones were imaged via μ CT with a voxel size of 20 μ m (eXplore CT 120, GE, Fairfield, CT, USA; 80 kVp, 32 μ A, 100 ms integration time). Obtained images were processed using Image J (version 1.50d). A gaussian filter of radius =1.00 was applied to minimize the noise present in the image. Later, a threshold was incorporated to the images to separate cortical bone tissue from non-mineralized tissue. A range of interest was selected to evaluate mechanical parameters of the samples. This region represents 2.5% of the entire bone length with the mid diaphysis located at the center of this representative volume. Lastly, CSA, moment of inertia (I), and centroids (coordinates x and y on CSA) were measured using an automated code and ImageJ plug-in, BoneJ (version 1.4.1; <http://bonej.org/>). From program output, the distance from the neutral axis to the bone surface was measured in order to calculate the section modulus.

3.Results

3.1 Body weight and fat pad mass

Through a 16-week diet treatment, male mice demonstrated higher weight gain and fat pad mass compared to female mice (Table 1). As previous studies suggest, male mice respond better to a high fat diet treatment than female mice[12]. As expected, high fat diet mice presented an increase in weight from the control group. This was observed on both male and female mice.

3.2 Geometrical properties

The geometrical properties of the femoral bones were measured using BoneJ. Figure 1(B) shows that male mice presented an average (CSA) of $.99\text{mm}^2$ (Chow), $.89\text{mm}^2$ (HFD) and $.94\text{mm}^2$ (HFD+FP) respectively. Preliminary results showed that the mice fed a HFD+FP possessed bones with higher cross-sectional area than mice fed control chow and HFD. On the other hand, female mice treatment groups presented an average cross-sectional area of $.60\text{mm}^2$ (Chow), $.73\text{mm}^2$ (HFD) and $.74\text{mm}^2$ (HFD+FP) as shown in Figure 1(B). In this case, type II diabetes mice demonstrated higher CSA than the control group. Type II diabetes patients have been known to possess higher bone mineral density than healthy patients. Lastly, male mice presented a higher value compared to female groups for moment of inertia in all experimental groups with $.177\text{mm}^4$ (Chow), $.175\text{mm}^4$ (HFD) and $.186\text{mm}^4$ (HFD+FP). Whereas in Figure 1(C), female mice presented moments of inertia values of $.082\text{mm}^4$ (Chow), $.114\text{mm}^4$ (HFD) and $.117\text{mm}^4$ (HFD+FP).

3.3 Mechanical Testing

Mechanical properties of femur bones were measured using 3-point bending. For these

results, there was no distinction between genders due to the small sample size. Figure 2(A) shows that the diet group exposed to *F. prausnitzii* has a higher bending moment. (B) No clear distinction can be made from tissue strength values. The two maximum strength values in Chow and HFD, respectively, belonged to female mice (Figure 2B).

4. Discussion

Female mice did not gain as much weight as male mice. Previous work has demonstrated that female mice do not respond as well to a high fat diet as male mice. It has also been proven that type II diabetes mice possess higher bone mineral density than healthy mice. This results in an underestimation of bone fracture risk[11]. The latter could be attributed to the increase in cross sectional area presented by the type II diabetes mice. In the same manner, mice that were exposed to FP demonstrated higher moment of inertia. Previous works have demonstrated that FP alters the gut microbiome[9]. Changing the gut microbiome has resulted in a change in the mechanical properties of the bone[2]. This could suggest that FP is, through some mechanism, counteracting the effects that type diabetes II has on the bone.

Preliminary results show that HFD+FP treatment group has a lower fracture risk than other two treatment groups. Due to the fact that FP can produce butyrate, the previous results could be attributed to butyrate's ability to regulate bone formation via T regulatory cell-mediated regulation. Previous studies found that this subpopulation of cells that are present in the immune system, can regulate bone formation by promoting differentiation of osteoblasts[13]. Two maximum values of

tissue strength on Figure 2(B) suggest that female mice are presenting a change in

composition of the bone tissue structure.

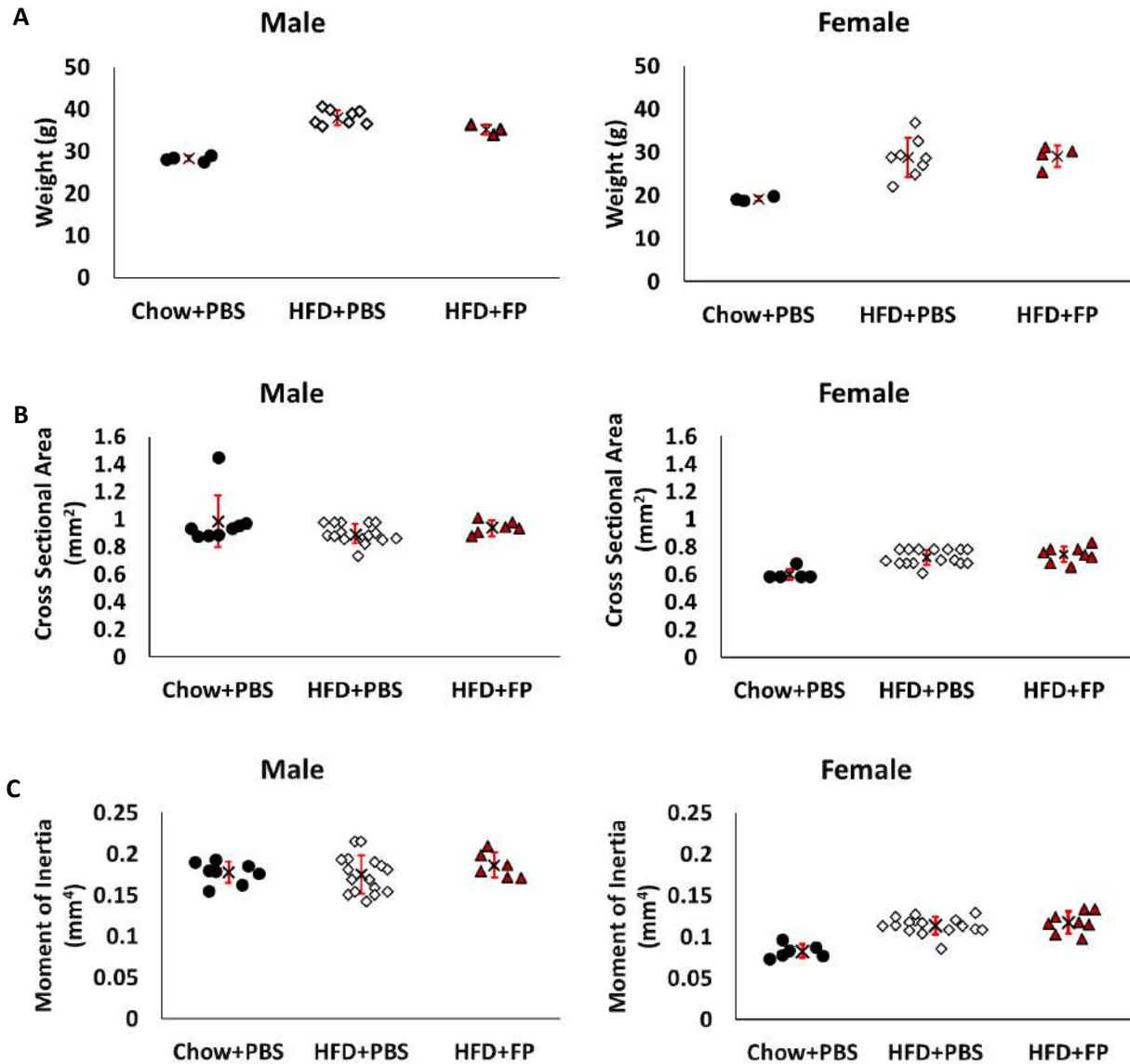


Figure 1: (A) Male mice presented higher body weight than female mice.(B) In both sex groups, mice that were exposed to FP, demonstrated higher cross sectional area than the other treatments.. (C) The moment of inertia was found to be noticeably greater in males than in female mice. Moreover, both groups exposed to FP showed higher values for moment of inertia than the other treatment groups.

Result	Male			Female		
	Chow+PBS	HFD+PBS	HFD+FP	Chow+PBS	HFD+PBS	HFD+FP
Weight(g)	28.3±.62	37.9±1.75	35.1±1.20	19.2±.50	28.8±4.5	29.07±2.5
CSA(mm ²)	0.98±.19	0.89±.07	0.94±.05	0.60±.04	0.73±.05	0.74±.06
Moment of Inertia(mm ⁴)	0.18±.01	0.17±.02	0.19±.01	0.083±.008	0.11±.01	0.12±.01

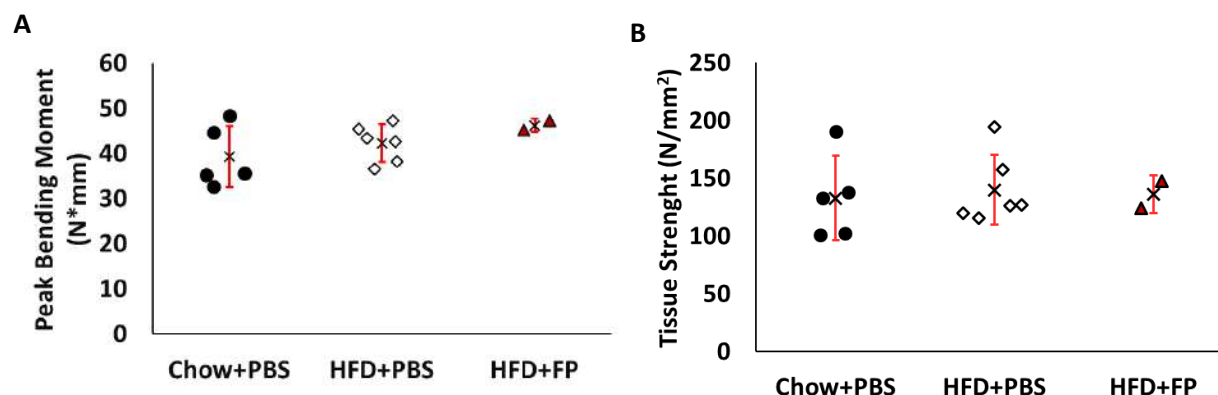


Figure 2: (A) Shows preliminary results for maximum moment. Mice that were exposed to FP demonstrated higher max load than other treatment groups. Which again could suggest that FP is decreasing fracture risk in type II diabetes mice. (B) Tissue strength values for broken samples were normalized by bone geometry. Preliminary results showed to maximum strength values pertaining to female mice in Chow and HFD treatment groups.

Conclusion

Preliminary results demonstrate that FP is stimulating bone formation. Mice exposed to *F. prausnitzii* presented higher values in CSA and moment of inertia. Mechanistic pathways for these effects are not presented in this study. Female mice presented higher bone tissue strength than male mice (although only two data points were presented). This suggest that cortical bone tissue in female mice is different from that in male mice. With preliminary data, we can conclude that there is a link between bacteria population in the host and bone

growth. Hypothetically, type II diabetes patients could be treated with *F. prausnitzii* to stimulate healthy bone formation and thus attaining better bone quality. This correlation could provide major insights on how to treat typeII diabetes patients from an orthopedics perspective.

References

- [1] I. Cho and M. J. Blaser, "The human microbiome : at the interface of health and disease," vol. 13, no. April, 2012.
- [2] J. D. Guss *et al.*, "Alterations to the Gut Microbiome Impair Bone

- Strength and Tissue Material Properties.”
- [3] L. A. David *et al.*, “Host lifestyle affects human microbiota on daily timescales,” pp. 1–15, 2014.
 - [4] E. H. Perspectives, “• Environmental Health Perspectives,” vol. 117, no. 5, 2009.
 - [5] K. Ganesan, S. K. Chung, J. Vanamala, and B. Xu, “Causal Relationship between Diet-Induced Gut Microbiota Changes and Diabetes : A Novel Strategy to Transplant *Faecalibacterium prausnitzii* in Preventing Diabetes,” 2018.
 - [6] C. J. Hernandez, J. D. Guss, M. Luna, and S. R. Goldring, “Links Between the Microbiome and Bone,” *Journal of Bone and Mineral Research*, vol. 31, no. 9. pp. 1638–1646, 2016.
 - [7] V. Der Meulen, A. Arbor, and I. Studies, “Changes in the Diaphyses of Long Bones,” vol. 30, no. 6, pp. 951–966, 2016.
 - [8] D. Vashishth, “Small animal bone biomechanics,” *Bone*, vol. 43, no. 5, pp. 794–797, 2008.
 - [9] E. Munukka *et al.*, “*Faecalibacterium prausnitzii* treatment improves hepatic health and reduces adipose tissue inflammation in high-fat fed mice,” *Nat. Publ. Gr.*, vol. 11, no. 7, pp. 1667–1679, 2017.
 - [10] C. Engdahl, P. Henning, U. H. Lerner, V. Tremaroli, M. K. Lagerquist, and F. Ba, “J BMR The Gut Microbiota Regulates Bone Mass in Mice,” vol. 27, no. 6, pp. 1357–1367, 2012.
 - [11] J. Starup-Linde, K. Hygum, and B. L. Langdahl, “Skeletal Fragility in Type 2 Diabetes Mellitus,” *Endocrinol. Metab.*, vol. 33, no. 3, p. 339, 2018.
 - [12] Y. Yang, D. L. Smith Jr, K. D. Keating, D. B. Allison, and T. R. Nagy, “Variations in body weight, food intake and body composition after long-term high-fat diet feeding in C57BL/6J mice,” *Obesity (Silver Spring)*, vol. 22, no. 10, pp. 2147–2155, Oct. 2014.
 - [13] A. M. Tyagi *et al.*, “The Microbial Metabolite Butyrate Stimulates Bone Formation via T Regulatory Cell-Mediated Regulation of WNT10B Expression,” *Immunity*, vol. 49, no. 6, pp. 1116-1131.e7, 2018.

Strain in Sr_2RuO_4 at the Fermi Liquid Crossover

Collin Sanborn

August 7, 2019

Strontium Ruthenate (Sr_2RuO_4) has been the topic of extensive research due to its unique superconducting properties. Above T_c (1.45K) and below T_{FL} (30K), Sr_2RuO_4 is a 3D Fermi liquid. Above T_{FL} , the Fermi liquid crossover temperature, Sr_2RuO_4 behaves as a metal. We propose this non-Fermi liquid behavior is due to nematic fluctuations that appear above the crossover temperature. Due to the fact that nematic order couples to strain of the same symmetry, we can validate our hypothesis through elastoresistivity measurements. Here, we detail finite-element simulations done to validate our intended measurement technique.

Introduction

Strontium Ruthenate has been a compelling material in superconductor research due to the possibility of observing a number of interesting phenomena including spin-triplet Cooper pairs and topological superconductivity^[1, 4, 7, 8, 9, 10, 12, 13]. Here, we utilize its value as a platform for studying nematic fluctuations, which may play an integral role in superconductivity. At T_{FL} (30K), Sr_2RuO_4 undergoes a poorly understood crossover from Fermi liquid to metal^[10], but the behavior of the elastic moduli give some insight into the physics behind this crossover. When cooling down from room temperature, most of the moduli of Sr_2RuO_4 stiffen as

expected. The B_{1g} modulus, however, softens at low temperatures, which leads us to believe the non-Fermi liquid behavior is driven by nematic fluctuations.

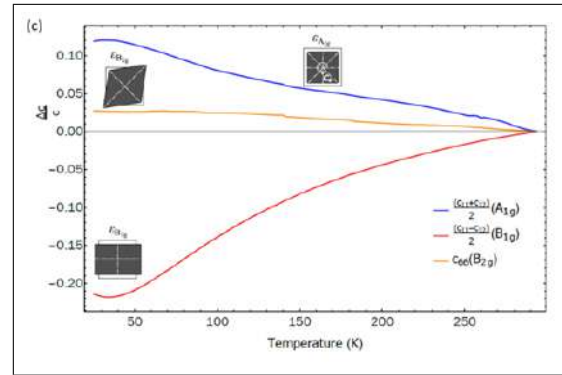


Figure 1: The change in the A_{1g} , B_{1g} , and B_{2g} elastic moduli of Sr_2RuO_4 when cooling from room temperature. A_{1g} and B_{2g} behave intuitively, but the softening of B_{1g} at low T is unexpected and yields insights into the material's behavior.

If the phase transition is driven by nematic fluctuations, we expect that there will be a large increase in the B_{1g} elastoresistance and nematic response at T_{FL} ^[2, 6]. Further, we expect that strain may act as a tuning parameter for T_{FL} , as similar results have been shown for other materials^[5, 3]. It is difficult to directly strain a Sr_2RuO_4 sample, and we intend to perform the necessary strain measurements on a sample affixed to a quartz substrate. It is not trivial to determine how the strain applied to the quartz relates to the strain felt by the

sample. In order to guide and verify the accuracy of these measurements, we utilize finite-element simulations to calculate strain and resistance profiles for the Sr_2RuO_4 crystal.

Methods

COMSOL Multiphysics was used to perform the finite-element simulations. Our system consists of a rectangular ($1000 \times 400 \times 30 \mu m$) Sr_2RuO_4 crystal affixed to the top of a quartz substrate with $1 \mu m$ of Loctite Stycast 2850 epoxy. This substrate is placed on top of two titanium blocks, which represent the strain cell used in the real measurement. Boundary conditions were imposed such that one block was fixed, and the other was displaced by a known amount. At the boundaries between materials, strain fields were assumed to be continuous. The quartz, epoxy, and titanium were all treated as isotropic materials for simplicity. Strontium ruthenate is a tetragonal crystal, and we orient its stiffness tensor such that the $[100]$ crystal direction is parallel to the x axis. In some later measurements, we transform the stiffness tensor with a 45 degree rotation so that the $[110]$ direction is along the x axis.

Additionally, the cooling from room temperature to 30K was simulated in order to include the strain induced by differences in thermal contraction between the materials. The displacement of one end of the quartz was parameterized and simulations were performed at 21 evenly spaced displacements between $-1 \mu m$ (compression) and $1 \mu m$ (tension). The components of the strain tensor were solved for locally. From these components, we consider three irreducible strain representations: $A_{1g} = \frac{1}{2}(\epsilon_{xx} + \epsilon_{yy})$, $B_{1g} = \frac{1}{2}(\epsilon_{xx} - \epsilon_{yy})$, and $B_{2g} = \epsilon_{xy}$. Additionally, we relate the strain and elastoresistivity tensors in order to calculate the local resistivities ρ_{ij} in the sample. Strontium Ruthenate belongs to the D_{4h} point group and its elastoresistivity tensor can therefore be simplified from 81 to 8 unique

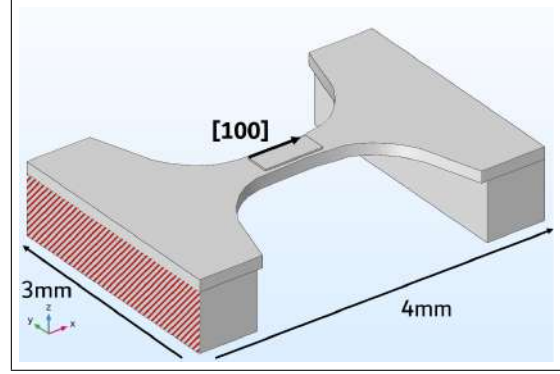


Figure 2: The quartz and Sr_2RuO_4 system. The Sr_2RuO_4 crystal is oriented such that the $[100]$ direction is oriented along the long axis of the quartz. The quartz crystal is approximately $4 \times 3 \times 0.25 mm$, and the Sr_2RuO_4 sample is $1000 \times 400 \times 30 \mu m$.

components^[11]. Using the equation $m_{ij,kl} = \frac{\partial(\Delta\rho/\rho)_{ij}}{\partial\epsilon_{kl}}$, where $(\Delta\rho/\rho)_{ij} = \frac{\Delta\rho_{ij}}{\sqrt{\rho_{ii}}\sqrt{\rho_{jj}}}$ we derive the following equations for the change in resistivity:

$$\begin{aligned} \left(\frac{\Delta\rho}{\rho}\right)_{xx} &= m_{xx,xx}\epsilon_{xx} + m_{xx,yy}\epsilon_{yy} + m_{xx,zz}\epsilon_{zz} \\ \left(\frac{\Delta\rho}{\rho}\right)_{yy} &= m_{yy,xx}\epsilon_{xx} + m_{yy,yy}\epsilon_{yy} + m_{yy,zz}\epsilon_{zz} \\ \left(\frac{\Delta\rho}{\rho}\right)_{zz} &= m_{zz,xx}\epsilon_{xx} + m_{zz,yy}\epsilon_{yy} + m_{zz,zz}\epsilon_{zz} \\ \left(\frac{\Delta\rho}{\rho}\right)_{yz} &= m_{yz,yz}(\epsilon_{yz} + \epsilon_{zy}) \\ \left(\frac{\Delta\rho}{\rho}\right)_{zx} &= m_{yz,yz}(\epsilon_{zx} + \epsilon_{xz}) \\ \left(\frac{\Delta\rho}{\rho}\right)_{xy} &= m_{xy,xy}(\epsilon_{xy} + \epsilon_{yx}) \end{aligned}$$

Results

We find that for A_{1g} and B_{1g} strain, there are large areas of uniform strain in the center of the sample, with some change near the edges. B_{2g} strain is 0 in the center of the sample and its orders of magnitude smaller everywhere else, and can therefore be disregarded. This is the result we hoped for, as the plots in Figure 3 give us a guide as to where to attach

contacts to the sample.

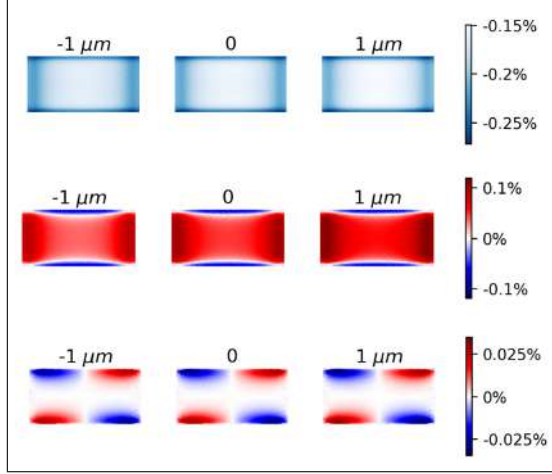


Figure 3: Plots of A_{1g} , B_{1g} , and B_{2g} strain at 3 simulated values of quartz displacement at 30K. Labels of the displacement appear above each plot. There are large uniform areas for A_{1g} and B_{1g} strain in the center of the sample. B_{2g} strain is an order of magnitude smaller and 0 in the center.

The shape of the strain profile remains unchanged from tension to compression, but the intensity of the profile changes as a function of applied displacement. A_{1g} strain increases in magnitude with compression, as expected since it is hydrostatic compression. B_{1g} strain, on the other hand, decreases in magnitude with compression. Figure 4, illustrates that in the central area of uniformity, strain changes uniformly as the quartz is displaced, and no correction to our measurement needs to be made for changes in the strain profile.

Comparing figures 3 and 4 shows that the largest contribution to the strain comes from thermal contraction, as the changes induced by the applied displacement are small relative to the strain at 0 displacement. It is worth verifying that there is a small, or no, height dependence in the strain profile, as significant changes in resistivity as a function of depth would be equally disruptive to our measure-

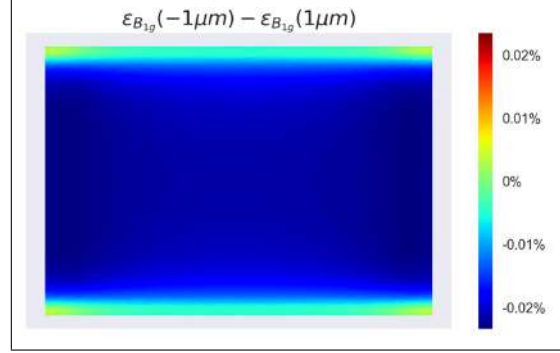


Figure 4: Plot of the difference in B_{1g} strain between $1\mu m$ compression and $1\mu m$ tension. The negative value of this plot shows that B_{1g} strain increases with tension.

ment technique. This is visualized in Figure 5.

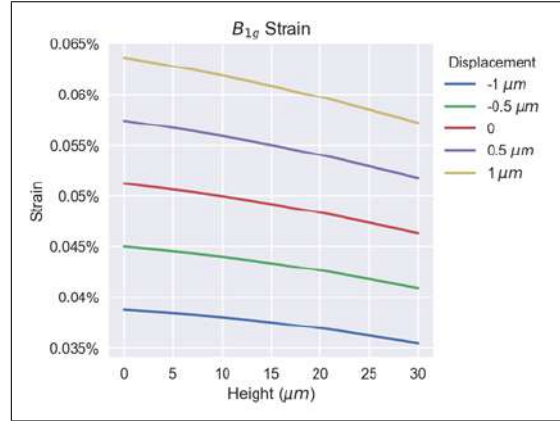


Figure 5: Plots of B_{1g} strain as a function of height, taken through the center of the sample. Looking at a single displacement, it can be seen that strain varies by only a few hundredths of a percent from top to bottom.

The B_{1g} strain varies by around 0.05% from top to bottom of the sample, and varies by very little in the top few microns, where most of the current will flow during measurement. Because of this, we don't expect any issues to arise due to vertical strain variation.

As part of the proposed measurement scheme, we will measure Sr_2RuO_4 with the [110] direction oriented along the same axis as strain. Figure 6 shows A_{1g} for the [100] and [110] directions side by side. There is around a 0.01% increase in the A_{1g} strain when swapping from [100] to [110] orientation. This change is very small, and verifies that we don't need to alter the way the measurement is taken when measuring the different orientation. When performing this shift in crystal orientation, in the frame of reference of the crystal, B_{1g} and B_{2g} will be swapped: the B_{1g} strain in the [100] orientation is the same as the B_{2g} strain in the [110] orientation.

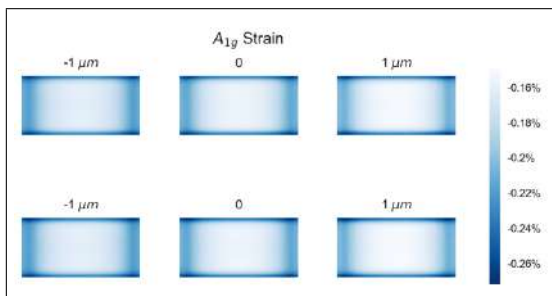


Figure 6: Maps of A_{1g} strain. [100] orientation is on top, and [110] orientation is below. As shown, there is little difference between the two orientations.

Using the equations described in methods, we calculate local maps for the change in resistivity. We use values for m_{ijkl} similar to those found for similar materials^[5]. It is possible to measure these values for strontium ruthenate to improve the value of our prediction, but here it is sufficient to verify that the profile remains uniform. We are most interested in the $(\frac{\Delta\rho}{\rho})_{xx}$ resistivity, as this is what we intend to measure. Figure 7 demonstrates the dependence of this parameter on the applied strain.

$(\frac{\Delta\rho}{\rho})_{xx}$ is uniform throughout large portions of the top surface of the Sr_2RuO_4 , which is promising for measurements. There is a noteworthy strain dependence, shown in the in dif-

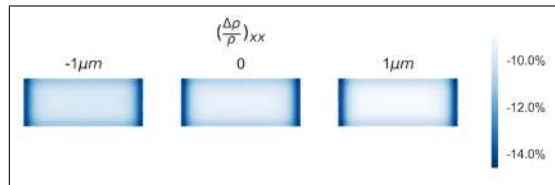


Figure 7: Maps of $(\frac{\Delta\rho}{\rho})_{xx}$ at 3 simulated values of quartz displacement at 30K. Each plot is labeled with the displacement above.

ference in $(\frac{\Delta\rho}{\rho})_{xx}$ from highest compression to highest tension ($\sim 2\%$). We see that compression leads to higher resistivities across all $(\frac{\Delta\rho}{\rho})_{ij}$. Tension counteracts the thermal contraction, while compression acts with it, leading to this effect.

Conclusion

Our finite-element simulations confirm the robustness of our proposed measurement techniques. Across all the simulations, we see large areas of uniform A_{1g} and B_{1g} strain, sufficient for the placement of contacts for a four-point measurement. There is not a significant strain dependence on sample thickness or crystal orientation, which may adversely impact the quality of our measurement. These simulations additionally offer a general guideline for what to expect in all strain measurements using our quartz and strain cell apparatus. The relationship between strain cell displacement and strain felt by the sample is of particular value to future measurements. We are now prepared to proceed with our measurements on real samples.

Acknowledgements

Thanks to Sayak Ghosh and Brad Ramshaw for their guidance and mentorship, as well as Florian Theuss for sharing his COMSOL experience.

Funding

This work was enabled by Cornell’s Center for Complex Materials Research and NSF Awards DMR-1752784 and DMR-1757420.

References

- [1] C. Bergemann et al. “Quasi-two-dimensional Fermi liquid properties of the unconventional superconductor Sr_2RuO_4 ”. In: *Advances in Physics* (2003). ISSN: 14606976. DOI: 10.1080/00018730310001621737.
- [2] Jiun Haw Chu et al. “Divergent nematic susceptibility in an iron arsenide superconductor”. In: *Science* (2012). ISSN: 10959203. DOI: 10.1126/science.1221713.
- [3] M. S. Ikeda et al. “Symmetric and antisymmetric strain as continuous tuning parameters for electronic nematic order”. In: *Physical Review B* (2018). ISSN: 24699969. DOI: 10.1103/PhysRevB.98.245133.
- [4] Catherine Kallin. “Chiral p-wave order in Sr_2RuO_4 ”. In: *Reports on Progress in Physics* (2012). ISSN: 00344885. DOI: 10.1088/0034-4885/75/4/042501.
- [5] Hsueh Hui Kuo et al. “Measurement of the elastoresistivity coefficients of the underdoped iron arsenide $\text{Ba}(\text{Fe}_{0.975}\text{Co}_{0.025})_2\text{As}_2$ ”. In: *Physical Review B - Condensed Matter and Materials Physics* (2013). ISSN: 10980121. DOI: 10.1103/PhysRevB.88.085113.
- [6] Hsueh Hui Kuo et al. “Ubiquitous signatures of nematic quantum criticality in optimally doped Fe-based superconductors”. In: *Science* (2016). ISSN: 10959203. DOI: 10.1126/science.aab0103.
- [7] Andrew Peter Mackenzie and Yoshiteru Maeno. *The superconductivity of Sr_2RuO_4 and the physics of spin-triplet pairing*. 2003. DOI: 10.1103/RevModPhys.75.657.
- [8] Yoshiteru Maeno, T. Maurice Rice, and Manfred Sigrist. “The Intriguing Superconductivity of Strontium Ruthenate”. In: *Physics Today* (2001). ISSN: 00319228. DOI: 10.1063/1.1349611.
- [9] Yoshiteru Maeno et al. *Evaluation of spin-triplet superconductivity in Sr_2RuO_4* . 2012. DOI: 10.1143/JPSJ.81.011009.
- [10] Yoshiteru Maeno et al. “Two-Dimensional Fermi Liquid Behavior of the Superconductor Sr_2RuO_4 ”. In: *Journal of the Physical Society of Japan* (1997). ISSN: 00319015. DOI: 10.1143/JPSJ.66.1405.
- [11] M. C. Shapiro et al. “Symmetry constraints on the elastoresistivity tensor”. In: *Physical Review B - Condensed Matter and Materials Physics* (2015). ISSN: 1550235X. DOI: 10.1103/PhysRevB.92.235147.
- [12] Y. Tada, N. Kawakami, and S. Fujimoto. “Pairing state at an interface of Sr_2RuO_4 : Parity-mixing, restored time-reversal symmetry and topological superconductivity”. In: *New Journal of Physics* (2009). ISSN: 13672630. DOI: 10.1088/1367-2630/11/5/055070.
- [13] V B Zabolotnyy, E Carleschi, and T K Kim. “Topological states in a correlated superconductor.” In: *arXiv* (2006). arXiv: arXiv:1103.6196v1.

Improving Battery Performance Using Porous, Organic Cathode Materials

Colleen Trainor^{1,2}, Brian Peterson², Brett Fors^{*2}

¹Department of Chemistry, Hillsdale College, Hillsdale, MI

²Department of Chemistry and Chemical Biology, Cornell University, Ithaca, NY

Abstract: Organic cathode materials provide an alternative to inorganic crystalline cathodes that are able to tolerate high rate of charging and discharging. This paper details the studies done to determine the correlation between surface area of N, N'-diphenyl phenazine-based polymers and rate performance. Two studies were done to test the hypothesis that capacity retention would increase as the surface area of the organic cathode material increased. The first study incorporates an nonplanar monomer, 2,2',7,7'-tetrabromospirobifluorene, into the polymerization. In the second study a synthesis is reported which increases the surface area of the polymer by conducting the polymerization in the presence of sodium chloride. The rate performance of the materials are determined by galvanostatic charge-discharge cycling at varying rates in a lithium half-cell.

I. Introduction

Due to the inherent tunability of organic substances and the natural abundance of organic elements, organic cathode materials provide a valuable alternative to crystalline, inorganic cathode materials for lithium ion batteries. Because of the structural versatility of organic materials, the capacities of batteries with organic cathodes can be increased by synthesizing polymers specifically designed to maximize the number of electrons transferred during cycling while minimizing the amount of non-redox active mass. The functional groups on the polymers can also be altered to shift the redox events to higher potentials—further increasing energy density of the resulting cathode.

The energy and power densities of traditional lithium ion batteries are limited by their metal oxide cathodes, which have capacities roughly half the amount of the typical anode material,

graphite. With crystalline structures, these inorganic cathodes resist the movement of the charge-balancing lithium ions through the cathode whereas polymer based cathodes, with relatively low intermolecular forces, present less resistance, allowing for faster battery charging and discharging. Additionally, amorphous organic cathode materials are more equipped than inorganic cathode materials to retain capacity at increasing rates of discharge.

In order to better increase ion mobility in the cathode, we hypothesized that increasing the porosity of polymers should improve the rate performance of the polymer within coin cells. Using phenazine-based polymers, which have already been shown to be high capacity, stable, cathode materials, we designed polymers with increased surface area and improved rate performance.¹⁻¹¹

II. Synthesis

Reduction of phenazine

Phenazine (4.0 g) and Na₂S₂O₄ (46.6 g) were added to a round bottom flask. Degassed ethanol (100 mL) and degassed water (400 mL) were then added. The solution was refluxed until the solution was all green. If the solution still had blue solid, the reflux was continued and roughly 100 mL additional ethanol was added. The product was then filtered off and washed with degassed water before being dried and stored under vacuum.

Synthesis of 2,2',7,7'-tetrabromo-9,9'-spirobifluorene¹²

A reaction tube was flame-dried with a stir bar and filled with nitrogen gas using standard Schlenk line techniques. All solid reagents were added (Br₂ = 5.0 equiv, FeCl₃ = 0.1 equiv, and 9,9'-spirobifluorene = 1.0 equiv.) The reaction tube was purged and backfilled three times with nitrogen gas. Chloroform (6 mL) was added at 0°C through a septum via needle syringe. The solution was warmed to room temperature and stirred for 3 h while venting into a solution of NaOH with positive pressure of nitrogen gas to prevent buildup of HBr gas. The solution was then washed with a saturated solution of sodium thiosulfate until no longer red. The aqueous layer was extracted with dichloromethane twice and the organic layers were combined and dried with magnesium sulfate. The product was recrystallized from ethanol and chloroform as white crystals.

Polymerizations using tetrabromospirobifluorene

Three polymerizations were run using varying amounts of tetrabromospirobifluorene and dibromobenzene (Table 1). Polymerizations

were performed under nitrogen atmospheres on a Schlenk line. Solids were added to a flame-dried, nitrogen-filled reaction vial with a stir bar (5,10-dihydrophenazine = 1.5 mmol, tribromobenzene = 0.75 mmol, NaOtBu = 3.2 mmol, RuPhos = 0.015 mmol, RuPhosPdG2 = 0.015 mmol)

	1	2	3
% Spirobifluorene	2%	5%	10%
% Dibromobenzene	23%	20%	15%
Spirobifluorene (mmol)	0.345	0.300	0.230
Dibromobenzene (mmol)	0.015	0.038	0.075

Table 1. Amounts of tetrabromospirobifluorene and dibromobenzene in polymerizations

The reaction tube was purged and backfilled three times with nitrogen. Toluene was added through a septum via needle syringe, and the reaction was placed in an oil bath at 110°C and stirred for 16 h.

Polymerizations containing NaCl¹³

A large reaction tube was flame-dried with a stir bar and filled with nitrogen gas on a Schlenk line. All solid reagents were added (5,10-dihydrophenazine = 1 mmol, tris(4-bromophenyl)amine = 0.66 mmol, NaOtBu = 2.2 mmol, RuPhos = 0.01 mmol, RuPhosPdG2 = 0.01 mmol.) The reaction tube was purged and backfilled with nitrogen three times. Tetrahydrofuran (THF)(30 mL), **3**, or Toluene (30 mL), **2**, was added through a septum via needle syringe. Toluene studies were stirred at 110°C for 42 h. THF studies were stirred at 60°C for 42 h. The product was then filtered off and washed with DCM, ethanol, methanol, and boiling water consecutively. The product was then resuspended and vortexed in 100 mL DCM and 100 mL water, filtered, and dried under vacuum at 65°C.

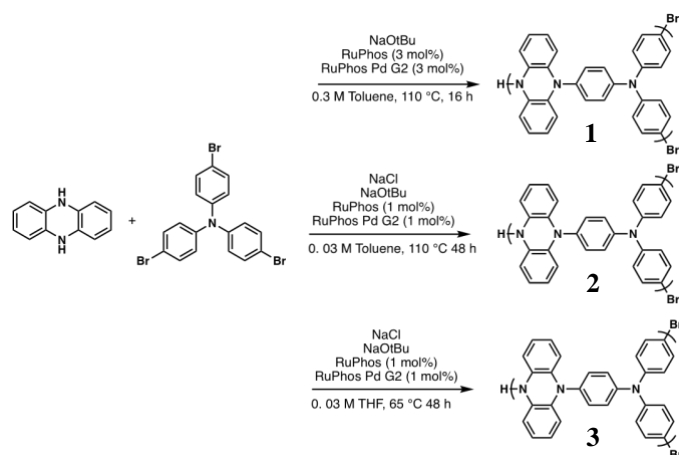


Figure 1. Synthesis conditions for three polymers: **1** without salt in toluene, **2** with NaCl in toluene, **3** with NaCl in THF

III. Results and Discussion

The spirobifluorene derivative 2,2',7,7'-tetrabromo-9,9'-spirobifluorene (SBF), a non-planar molecule, was synthesized from 9,9'-spirobifluorene and polymerized with phenazine, 1,4-dibromobenzene, and 1,3,5-tribromobenzene. It was expected that polymerization using a non-planar monomer would lead to an increase in the surface area of the polymer. Increasing the surface area of the polymer may allow for improved accessibility to the phenazine units on the interior of the material, better enabling the movement of lithium ions.

The Abruña group created coin-cells containing these polymers, carbon black, and a Polyvinylidene difluoride binder in a 6:3:1 ratio, and ran charge/discharge tests on the coin-cells. Although the surface area of the polymers synthesized with SBF is still unknown, rate data shows a decrease in rate performance with increasing amounts of SBF copolymerized (Figure 2). If the polymers display greater surface area with incorporation of SBF, then this result would be in disagreement with the hypothesis.

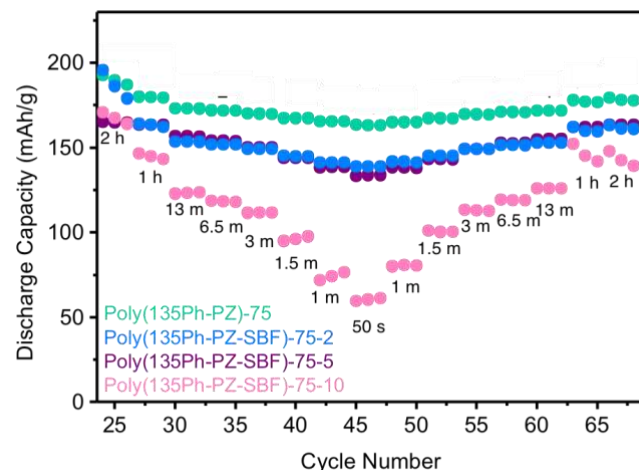


Figure 2. Discharge capacity of SBF containing coin cells discharged at increasing rates

The Faul group from the University of Bristol reported that incorporating a salt into the solvent during polymerization creates porous polymers.² For our studies, NaCl was used as the salt in the polymerization of phenazine and tris(4-bromophenyl)amine. Polymers **1**, **2**, and **3** were successfully synthesized and porosity measurements showed that the addition of salt to the solvent during the syntheses of **2** and **3** did increase the surface area of the polymers (Table 2).

	Solvent	NaCl	Surface Area
1	Toluene	No	0 m ² g ⁻¹
2	Toluene	Yes	213 ± 43 m ² g ⁻¹
3	THF	Yes	782 ± 41 m ² g ⁻¹

Table 2. Surface area data from polymers **1**, **2**, and **3**

Coin cells containing polymer **3**, which has the highest surface area, performed best in rate performance testing. As the surface area of the polymers increased, the rate performance improved, supporting the hypothesis that there is a direct correlation between increasing polymer surface area and increasing rate performance.

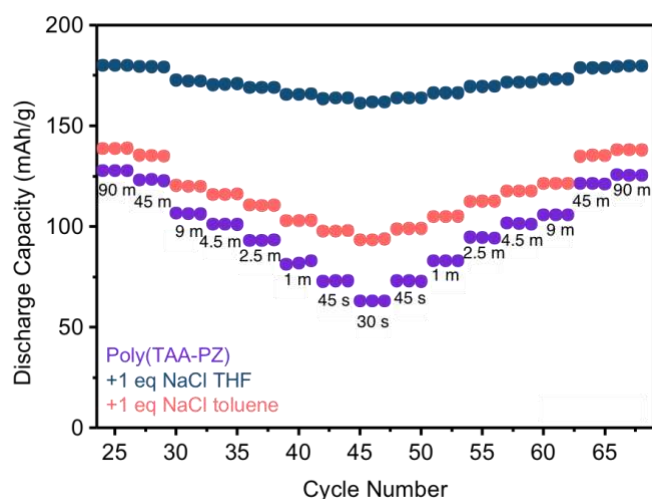


Figure 3. Discharge capacity of salt study polymers in coin cells being discharged at varying rates

IV. Conclusion

The results of the salt studies are in agreement with the hypothesis that increasing the surface area of the polymers in the cathodes of the coin cells increases the rate performance of the batteries. However, the copolymerization of tetrabromospirobifluorene, which was expected to increase the surface area of the polymer, reduced the capacity retention of the coin cell.

V. Acknowledgements

I would like to thank the NSF (DMR-1757420) and the Cornell Center for Materials Research (CCMR) for funding my work as well as Dr. Brett Fors, Brian Peterson, and the whole Fors group. Additional thanks goes to the CCMR REU students for their help and support.

Reference

[1] S.-Y. Yang, Y.-J. Chen, G. Zhou, Z.-W. Fu, *J. Electrochem. Soc.* **2018**, 165, A1422-A1429.

[2] J. Wang, K. Tee, Y. Lee, S. N. Riduan, Y. Zhang, *J. Mater. Chem. A* **2018**, 6, 2752-2757.
 [3] T. Matsunaga, T. Kubota, T. Sugimoto, M. Satoh, *Chem. Lett.* **2011**, 40, 750-752.
 [4] Hollas, X. Wei, V. Murugesan, Z. Nie, B. Li, D. Reed, J. Liu, V. Sprenkle, W. Wang, *Nat. Energy* **2018**, 3, 508-514.
 [5] Peng, G.-H. Ning, J. Su, G. Zhong, W. Tang, B. Tian, C. Su, D. Yu, L. Zu, J. Yang, *Nat. Energy* **2017**, 2, 17074.
 [6] J. Wang, C. S. Chen, Y. Zhang, *ACS Sustain. Chem. Eng.* **2017**, 6, 1772.
 [7] G. Dai, X. Wang, Y. Qian, Z. Niu, X. Zhu, J. Ye, Y. Zhao, X. Zhang, *Energy Storage Materials* **2019**, 16, 236-242.
 [8] J. A. Kowalksi, M. D. Casselman, A. P. Kaur, J. D. Milshtein, C. F. Elliot, S. Modekrutti, N. H. Attanayake, N. Zhang, S. R. Parkin, C. Risko, F. R. Brushett, S. A. Odom, *J. Mater. Chem. A* **2017**, 5, 24371-24379.
 [9] P. Kaur, C.F. Elliot, S. Ergun, S. A. Odom, *J. Electrochem. Soc.* **2016**, 163, A1-A7.
 [10] B. M. Peterson, C. N. Gannett, L. Shen, J. Seok, B. P. Fors, H. D. Abruña, The Effects of Cross-linking on Capacity, Stability, and Rate Capabilities in Phenazine-Based Polymer Cathodes. *Manuscript in preparation*.
 [11] B. M. Peterson, D. Ren, L. Shen, Y. M. Wu, B. Ulgut, G. W. Coates, H. D. Abruña, B. P. Fors, *ACS Appl. Energy Mater.* **2018**, 32, 4244-4249.
 [12] R. Wu, J. S. Schumm, D. L. Pearson, J. M. Tour, *J. Org. Chem.* **1996**, 61, 20, 6906-6921.
 [13] J. Chen, W. Yan, E. J. Townsend, J. Feng, L. Pan, V. Del Angel Hernandez, C. F. Faul, *Angew. Chemie Int. Ed.* **2019**, 58.

Using Machine Learning to Create a New Quantum Chemistry Approximation

Dzmitry Vaido,^{†,‡} Brian G. Ernst,[†] Zachary M. Sparrow,[†] Richard Kang,[†] and
Robert A. DiStasio Jr.^{*,†}

[†]*Department of Chemistry & Chemical Biology, Cornell University, Ithaca, USA*

[‡]*Department of Physics & Astronomy, Louisiana State University, Baton Rouge, USA*

E-mail: dv273@cornell.edu

Abstract

In this paper we present a procedure for building an 18-parameter, range-separated hybrid, generalized gradient approximation density functional approximation with non-local correlation. The functional is based on a popular ω B97X-V functional. We increased the number of parameters and used the linearity of some of them for a more efficient optimization procedure. The preliminary results of the optimization were compared to ω B97X-V functional. We also built an extensive and diverse database for further training of the functional.

Introduction

Quantum chemistry focuses on the development of methods to obtain all properties of chemical systems using the basic principles of quantum mechanics. This allows us to model experiments in chemistry on the computer. Calculations require less time and resources than synthesis of actual molecules with following experimental measurements. However,

accurate physical models are essential for designing new drugs, fertilizers, catalysts, and other chemicals. Therefore, there is an acute need for faster and more precise computational techniques.

Currently, there are two main approaches to deal with the electronic problem in computational chemistry. One is to solve the Schrödinger equation for a multi-electron wavefunction, which is in principle exact, but is very computationally expensive. The other popular method is Density Functional Theory (DFT), where instead of dealing with multi-electron wavefunction, one considers the electronic density. DFT is faster, but unfortunately less accurate.

Our goal is to build a new density functional approximation, which would be comparable in accuracy to full wavefunction calculations.

Theory

In DFT energy can be expressed in the following form:

$$\begin{aligned} E_{DFT} &= T + E_{NN} + E_{eN} + E_{ee} \\ &= T_s + E_{NN} + E_{eN} + J + E_{xc} \end{aligned}$$

where T is the kinetic energy of electrons, E_{NN} is nucleus-nucleus repulsion, E_{eN} is electron-nucleus attraction, E_{ee} is electron-electron repulsion, T_s is Kohn-Sham kinetic energy and J is Coulomb interaction. There are exact expressions for E_{NN} and E_{eN} (assuming Born-Oppenheimer approximation), while exact expressions for T and E_{ee} are unknown. The common way of dealing with that is to approximate the kinetic energy by Kohn-Sham kinetic energy and electron-electron repulsion by Coulomb interaction, then associated error is combined in a term called exchange-correlation energy:

$$E_{xc} = (T - T_s) + (E_{ee} - J)$$

Unfortunately, there is no known method that can get E_{xc} exactly, but by the Hohenberg-Kohn theorems it is some functional of electron density. Most of the research in the area is aimed to get more accurate approximations for it. In this paper we explore the use of machine learning to obtain a better E_{xc} functional. The idea is to parametrize E_{xc} and then use a database with high quality densities and reference energies to train our functional on it, meaning find the best parameters to match the reference data. After training, we test the resulting E_{xc} functional on a different dataset to estimate its performance and compare it to existing functionals. We choose to parametrize Exc according to the ω B97X-V model:

$$E_{xc} = E_{x, sr}^{B97} + E_x^{exact} + E_{c, ss}^{B97} + E_{c, os}^{B97} + E_{c, nl}^{VV10}$$

where $E_{x, sr}^{B97}$ is short range exchange, E_x^{exact} is exact exchange, $E_{c, ss}^{B97}$ is same spin correlations, $E_{c, os}^{B97}$ is opposite spin correlations, and $E_{c, nl}^{VV10}$ is non-local correlations. $E_{x, sr}^{B97}$ has the following form:

$$E_{x, sr}^{B97} = \sum_{\sigma}^{\alpha, \beta} \int -\frac{3}{2} \left(\frac{3}{4\pi} \right)^{1/3} \rho_{\alpha}^{4/3} F(a_{\sigma}) \sum_{i=0}^m c_{x, i} \left[\frac{\gamma_x s_{\sigma}^2}{1 + \gamma_x s_{\sigma}^2} \right]^i d\vec{r}$$

where $a_{\sigma} = \frac{\omega}{k_{F\sigma}}$ and ω is nonlinear parameter and F is a multiplicative attenuation function, while $c_{x, i}$ are linear parameters (m can go up to 5). To be able to explore the linearity of the parameters, we needed to move them outside of the integral, then every parameter has a corresponding integral of the form:

$$E_{x, sr, i}^{B97} = c_{x, i} \sum_{\sigma}^{\alpha, \beta} \int -\frac{3}{2} \left(\frac{3}{4\pi} \right)^{1/3} \rho_{\alpha}^{4/3} F(a_{\sigma}) \left[\frac{\gamma_x s_{\sigma}^2}{1 + \gamma_x s_{\sigma}^2} \right]^i d\vec{r}$$

which could be evaluated for every geometry and then used for least-square fitting. Both $E_{c, ss}^{B97}$, and $E_{c, os}^{B97}$ had a similar form, which means we could explore the linearity of their corresponding parameters (up to 5 for each). Beside ω and these 15 linear parameters, there is an additional linear parameter for exact exchange, and two more nonlinear parameters for non-local correlations. There is also one constraint linear parameters, so there are up to 15

linear and 3 nonlinear independent parameters total.

Database

To choose them appropriately, we trained this functional on an extensive and diverse database. In total, two training sets and the testing set contained 12000 data points. The training sets and the testing set contain thermochemistry data, nonequilibrium noncovalent interactions data, nonequilibrium molecular geometries, electron and proton affinities, barrier heights, polarizabilities and other data.

Training

To train the functional we use multifidelity optimization for Root Mean Square Error in calculated energies: the low fidelity loop consists of one iteration that uses densities from PBE0 and one iteration to compute energy from that density, and the high fidelity loop that uses the self-consistent field to compute energy. The high fidelity loop gives us the idea of where precisely in 18-dimensional space of all our parameters the error minima are located, while the low fidelity loop, which is about three orders of magnitude cheaper, provides the shape of the surface, allowing us to interpolate the points obtained in the high fidelity loop.

The database was split into the training set and the testing set. We used the geometries from the whole training set in the low fidelity loop, and the selected geometries from this set in the high fidelity loop. The testing set is used for the validation of the final functional and is different from the training set to check for transferability.

Result and discussion

To verify our optimization scheme we trained our functional on 63 water dimers. We kept all nonlinear parameters fixed and found the optimal linear parameters using least-square

fit. The first set of preliminary results of the training were compared to ω B97X-V in the table below:

Error	ω B97X-V	Our Functional
MAE, kcal/mol	0.0668	0.0231
RMESE, kcal/mol	0.0901	0.0301

As we can see from the table, our procedure does allow us to minimize the error. This means that we can continue our training on larger datasets.

Conclusion

Our preliminary results show that our technique can be used to improve the existing ω B97X-V functional. Now our plans are to continue that training procedure on the whole database. To optimize the parameters we will be using two-level fidelity co-kriging.

Acknowledgement

The authors thank Lijie Tu and Yang Yang for useful comments and discussions. A special thanks to the CCMR REU program for making this experience possible. This work was supported by the NSF under the award number DMR-1757420.

References

- (1) N. Mardirossian and M. Head-Gordon, *Phys. Chem. Chem. Phys.*, 2014, **16**, 9904-9924.
- (2) A. Becke, *J. Chem. Phys.*, 1997, **107**, 8554.
- (3) M. Xiao, G. Zhang, P. Breitenkopf, P. Villon, W. Zhang, *Appl. Math. Comput.*, 2018, **323**, 0096-3003.

- (4) Szabo, A., Ostlund, N. S. (1996). *Modern quantum chemistry: Introduction to advanced electronic structure theory*. Mineola, N.Y: Dover Publications.
- (5) Koch, W., Holthausen M. C. (2001). *A Chemist's Guide to Density Functional Theory*. WileyVCH Verlag GmbH.